The Radiogenomic Risk Score: Construction of a Prognostic Quantitative, Noninvasive Image-based Molecular Assay for Renal Cell Carcinoma[1]

Neema Jamshidi, MD, PhD
Eric Jonasch, MD
Matthew Zapala, MD, PhD
Ronald L. Korn, MD, PhD
Lejla Aganovic, MD
Hongjuan Zhao, PhD
Raviprakash Tumkur Sitaram, DVM
Robert J. Tibshirani, PhD
Sudeep Banerjee, MD
James D. Brooks, MD
Borje Ljungberg, MD
Michael D. Kuo, MD

Purpose: To evaluate the feasibility of constructing radiogenomic-based surrogates of molecular assays (SOMAs) in patients with clear-cell renal cell carcinoma (CCRCC) by using data extracted from a single computed tomographic (CT) image.

Materials and Methods: In this institutional review board approved study, gene expression profile data and contrast material–enhanced CT images from 70 patients with CCRCC in a training set were independently assessed by two radiologists for a set of predefined imaging features. A SOMA for a previously validated CCRCC-specific supervised principal component (SPC) risk score prognostic gene signature was constructed and termed the radiogenomic risk score (RRS). It uses the microarray data and a 28-trait image array to evaluate each CT image with multiple regression of gene expression analysis. The predictive power of the RRS SOMA was then prospectively validated in an independent dataset to confirm its relationship to the SPC gene signature ($n = 70$) and determination of patient outcome ($n = 77$). Data were analyzed by using multivariate linear regression–based methods and Cox regression modeling, and significance was assessed with receiver operator characteristic curves and Kaplan-Meier survival analysis.

Results: Our SOMA faithfully represents the tissue-based molecular assay it models. The RRS scaled with the SPC gene signature ($R = 0.57$, $P < .001$, classification accuracy 70.1%, $P < .001$) and predicted disease-specific survival (log rank $P < .001$). Independent validation confirmed the relationship between the RRS and the SPC gene signature ($R = 0.45$, $P < .001$, classification accuracy 68.6%, $P < .001$) and disease-specific survival (log-rank $P < .001$) and that it was independent of stage, grade, and performance status (multivariate Cox model $P < .05$, log-rank $P < .001$).

Conclusion: A SOMA for the CCRCC-specific SPC prognostic gene signature that is predictive of disease-specific survival and independent of stage was constructed and validated, confirming that SOMA construction is feasible.

Online supplemental material is available for this article.

An earlier incorrect version of this article appeared online. This article was corrected on August 24, 2015.

[1] From the Department of Radiological Sciences, David Geffen School of Medicine at UCLA, Box 951721, CHS 17-135, 10833 LeConte Ave, Los Angeles, CA 90095-1721 (N.J., M.Z., S.B., M.D.K.); Department of Genitourinary Medical Oncology, The University of Texas M.D. Anderson Cancer Center, Houston, Tex (E.J.); Department of Radiology, Hospital of Veterans Affairs, University of California–San Diego, San Diego, Calif (M.Z., L.A.); Scottsdale Medical Imaging, Scottsdale, Ariz (R.K.); Department of Urology, Stanford University School of Medicine, Stanford, Calif (H.Z., J.D.B.); Department of Surgical and Perioperative Sciences, Urology and Andrology, Umea Hospital, Umea, Sweden (R.T.S., B.L.); and Department of Statistics, Stanford University, Stanford, Calif (R.J.T.). Received April 3, 2015; revision requested May 15; revision received June 4; accepted June 12; final version accepted June 30. S.B. supported by a Society of Interventional Radiology Foundation Student Research Grant. **Address correspondence to** M.D.K. (e-mail: *Michaelkuo@mednet.ucla.edu*).

Although much attention has recently been focused on molecular profiling of tumor cells as a means to facilitate development of prognostic and predictive biomarkers, there are inherent limitations to such approaches, including the often lack of a coherent biologic interpretation of the molecular phenotypes and the invasiveness of the tissue acquisition process, which also limits the frequency and number of samples that can be acquired over time (1–3). Additionally, although genomic profiling is able to account for outcome differences that histopathologic analysis cannot, it suffers from the intrinsic limitations of tissue sampling common to all tissue-based assays that often fails to adequately capture the full scope of the disease phenotype (3). Furthermore, recent studies have revealed that even tumor cells with the same genotype can have disparate phenotypes (4). Clearly, a test that is able to incorporate both clinically relevant genomic, as well as macroscopic functional and physiologic scale phenotypic, information into a single noninvasive assay would be of tremendous value.

Radiogenomics have been shown to be a powerful approach for associating genome scale information with macroscopic phenotypes captured with noninvasive imaging (5–9). Imaging data can capture information about molecular characteristics as well as the functional organization of cells and tissues. Clinical imaging phenotypes, or radiophenotypes, represent the summation of complex imaging features that account for physiologic and molecular interactions in the context of hierarchically organized cells, tissues, and organs. Whether radiogenomics can be used to systematically construct new quantitative or semiquantitative radiophenotypes de novo, which track complex quantitative molecular phenotypes in addition to systems-level phenotypic information not afforded by genomics, is a fundamental question that remains largely unknown. Because radiophenotypes capture three-dimensional spatial organization and interactions between different cellular populations and their microenvironments, there is information contained in the imaging appearance of the tumors that cannot be accounted for by the genomic profiles alone. Moreover, this is a question of great practical importance because cross-sectional imaging is the cornerstone of solid tumor treatment decision making, and the ability to measure surrogates of molecular phenotypes with noninvasive imaging could greatly impact the decision making process.

We hypothesized that radiogenomics-based surrogates of molecular assays (SOMAs) that track targeted molecular phenotypes and quantitative molecular assays in patients with clear-cell renal cell carcinoma (CCRCC) could be designed. To address this challenge, we first set out to assess the feasibility of de novo reconstruction of a predefined complex quantitative multigene assay by using only data extracted from routine computed tomographic (CT) images and employing a radiogenomics-based approach. We focused on CCRCC and the previously validated supervised principal component (SPC) risk score, a quantitative multigene assay that consists of 259 genes whose expression was previously shown to predict disease-specific survival in patients with CCRCC independent of disease stage, disease grade, and performance status (10). We constructed a SOMA termed the radiogenomic risk score (RRS), which quantitatively tracks the SPC gene signature and was predictive of outcome in a training set of 70 patients, then validated it in an independent set of 70 prospectively collected patients.

Advances in Knowledge

- It is possible to systematically design noninvasive surrogates of molecular assays (SOMAs) that bridge the gap between quantitative tissue-based molecular assays, clinical imaging findings, and clinical phenotypes.
- A SOMA for a clear-cell renal cell carcinoma prognostic multigene signature, termed a radiogenomic risk score, was trained (n = 70) and validated (n = 77) in independent data sets and shown to predict disease-specific survival, independent of disease stage, disease grade, and performance status (multivariate Cox model, $P < .05$ and log-rank $P < .001$).

Implication for Patient Care

- Complex, multifeature radiogenomic biomarkers that efficiently describe associations with prespecified quantitative molecular phenotypes as well as systems-level phenotypes not accessible by genomic-based tests alone can be constructed, with a range of potential clinical applications, including prognostication and patient stratification in human clinical trials.

Materials and Methods

Patients and Materials

Archived fresh frozen tissue samples, clinical data, and results of imaging studies performed as part of routine clinical care were analyzed, with approval by

Published online before print
10.1148/radiol.2015150800 **Content codes:** CT GU

Radiology 2015; 277:114–123

Abbreviations:
CCRCC = clear-cell renal cell carcinoma
cDNA = complementary DNA
ROC = receiver operating characteristic
RRS = radiogenomic risk score
SOMA = surrogate of molecular assays
SPC = supervised principal component
WHO = World Health Organization

Author contributions:
Guarantors of integrity of entire study, N.J., M.D.K.; study concepts/study design or data acquisition or data analysis/interpretation, all authors; manuscript drafting or manuscript revision for important intellectual content, all authors; approval of final version of submitted manuscript, all authors; agrees to ensure any questions related to the work are appropriately resolved, all authors; literature research, N.J., M.Z., J.D.B., M.D.K.; clinical studies, N.J., E.J., R.K., L.A., R.T.S., J.D.B., B.L., M.D.K.; experimental studies, E.J., R.K., S.B., J.D.B., M.D.K.; statistical analysis, N.J., M.Z., R.J.T., M.D.K.; and manuscript editing, N.J., E.J., R.K., S.B., J.D.B., M.D.K.

Conflicts of interest are listed at the end of this article.

Figure 1

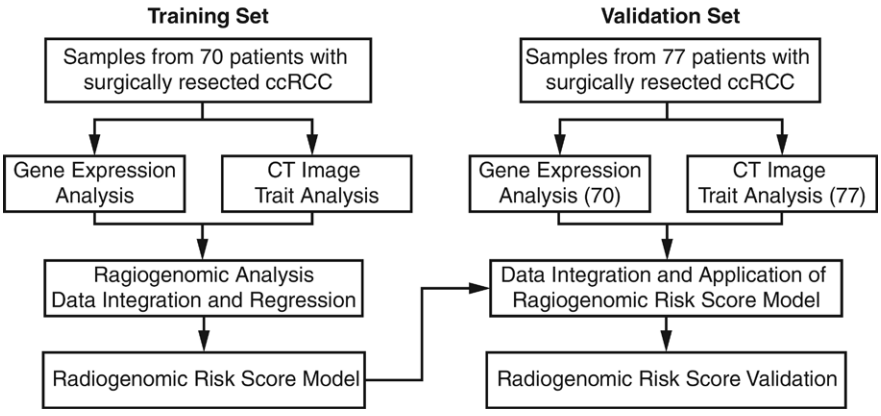

Figure 1: Diagram shows the study design, construction of the RRS predictor, and analysis workflow of the training and testing data sets.

Table 1

Patient Distribution between Training and Validation Test Sets

Characteristic	No. in Training Set	No. in Validation Set	*P* Value
Sex			.77
Male	39	41	…
Female	31	36	…
Age (y)	67 (42–85)	65 (34–87)	.34
Disease stage			.61
1	21	32	…
2	17	7	…
3	11	17	…
4	21	21	…
Disease grade			.60
1	6	9	…
2	19	25	…
3	34	28	…
4	11	15	…
WHO classification			.54
0	34	30	…
1	17	28	...
2	16	14	…
3	3	5	…
Median follow-up (mo)	63 (2–156)	71 (1–123)	.39
No. disease-specific deaths	32	29	.33

Note.—Except where indicated, data are numbers of patients, and data in parentheses are the range. WHO = World Health Organization.

the local institutional review boards of Umea University Hospital and in compliance with the Declaration of Helsinki. The training set used to construct the RRS consisted of CCRCC tumors from 70 consecutive patients treated with radical nephrectomy between 1994 and 2003 at Umea University Hospital for whom fresh frozen tissue, clinical outcomes, and matched preoperative diagnostic contrast material–enhanced CT images were available (Appendix E1 [online]). The validation set consisted of a prospectively collected set of 77 consecutive patients with CCRCC who underwent radical nephrectomy between 2000 and 2007 at Umea University Hospital for whom data on clinical outcomes, fresh frozen tissue and matched preoperative contrast-enhanced CT images were available; of these 77 patients, fresh frozen tissue were available for gene expression analysis in 70. The overall study design is shown in Figure 1, and the patient characteristics of the training and validation sets are described in Table 1.

Approach

We devised a three-step procedure for creating a noninvasive image-based surrogate for the SPC risk score in a training set of 70 patients with CCRCC that ranged from stage 1 to stage 4 with CT and complementary DNA (cDNA) gene expression profiling data (Fig 2). First, we developed a gene signature based on the CCRCC-specific SPC risk score that was previously developed by Zhao et al (10) (Table E1 [online]). Second, we designed a custom library of CT features that capture various aspects of tumor physiologic and morphologic characteristics, tumor microenvironment, and local tumor-parenchyma ecologic characteristics, which would enable the subsequent construction and identification of RCC radiophenotypes (Appendix E1 [online]). The interpreting radiologists independently assessed each patient's CT image against the entire image feature library (Table E2 [online]). Finally, to create a stage-independent image-based predictor similar to that of Zhao et al, stage-related traits were removed, and multivariate linear regression was performed between the top eigenvector of the patient-wise gene expression distance matrix (which was independently correlated with patient outcome) and the top stage-independent image traits (Appendix E1 [online]), accounting for the greatest variance in SPC gene expression (11). The resultant quantity, termed the RRS, defined the relationship between expression of the genes of the SPC risk score and the expression of the composite CT image phenotype (radiophenotype) and constituted our targeted, noninvasive molecular

Figure 2

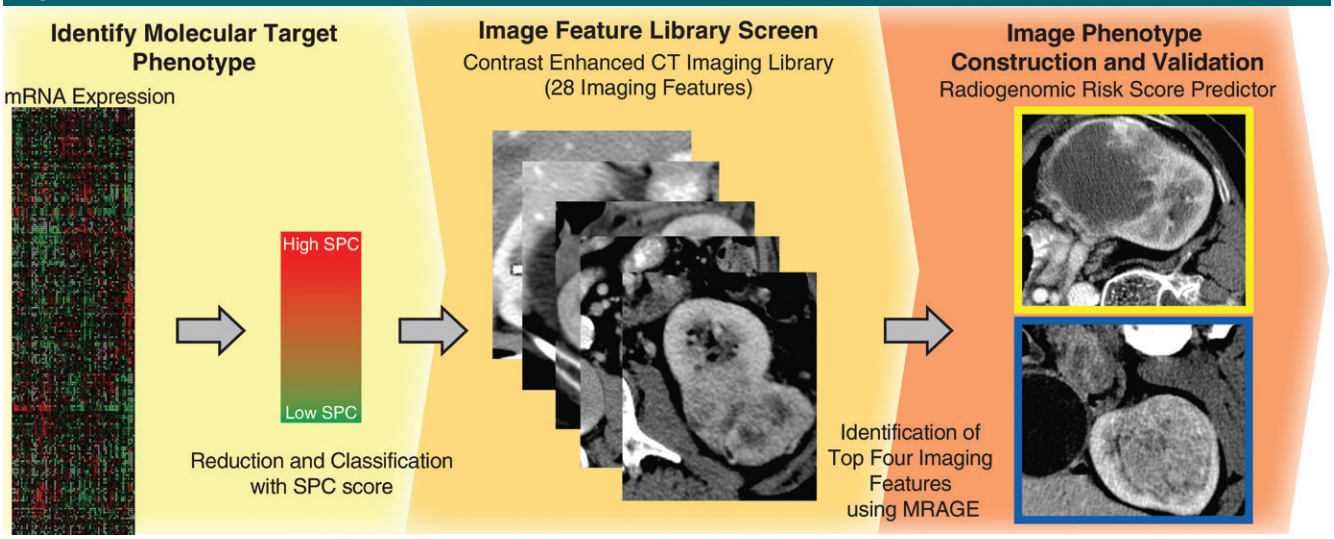

Figure 2: Diagram shows the three-step process for constructing an RRS, a targeted semiquantitative image-based assay based on the SPC risk score. First, a target phenotype is identified. In our analysis, we use the SPC risk score as the target phenotype to classify patients. Next, a CT feature library is screened against patient CT data. Finally, the image phenotype is constructed after the optimum set of imaging features is identified to account for variance of the expression matrix, followed by multivariate regression, which is used to create the RRS from the top image traits; the RRS radiophenotype is then validated (11). *MRAGE* = multivariate regression analysis of gene expression.

assay (SOMA). Once the RRS was constructed, we performed prospective validation of the RRS in an independent data set (Appendix E1 [online]).

Gene Expression Profiling

For the training set, gene expression profiles of the 70 CCRCCs (performed on cDNA microarrays that contained over 40 000 cDNA clones and represented 27 290 unique UniGene clusters) were accessed and filtered to only those genes that were most variably expressed and well measured (Appendix E1 [online]), a process that was previously described (10). The subset of transcripts that mapped to the SPC signature was subsequently extracted for construction of the RRS. For the validation set, fresh frozen tissue was available for 70 samples. Total RNA was isolated from the CCRCC tissue samples by using TRIzol (Invitrogen; Carlsbad, Calif), and RNA integrity was assessed by using a 2100 Bioanalyzer (Agilent Technologies; Palo Alto, Calif). Only specimens with *(a)* more than 1 mg of high-quality total RNA determined with the standard 260/280 ratio of absorbance greater than 2.0 per sample and *(b)* an RNA integrity number greater than 6 were used. All 70 samples passed this filtering measure. Gene expression profiles of the 70 CCRCCs were created on Illumina Human HT-12 v4 Expression BeadChip arrays (Illumina, San Diego, Calif), which contain 47 231 probes. Quantile normalization was performed with the lumi R package (12). The expression arrays were filtered on the basis of the set of SPC transcripts that mapped to the Illumina probes.

CT and Image Feature Analysis

Diagnostic contrast material–enhanced CT images were obtained with single- or four-section CT (Light-Speed; GE Healthcare, Waukesha, Wis) within 4 weeks prior to the time of surgery by using 5- or 10-mm collimation with 2.5- or 5-mm reconstruction. Images were acquired with either a triphasic renal protocol or a single-phase technique. For the triphasic renal protocol, images were obtained 30, 50, and 70 seconds after the start of intravenous injection of ioversol at a rate of 5 mL/sec. For the single-phase technique, images were obtained 60–70 seconds after the start of ioversol injection at a rate of 2–3 mL/sec.

As was previously described, 35 distinct imaging traits containing structural, compositional, physiologic, and functional information were scored across all tumor samples (Table E2 [online]) (5,8,13). Readers were trained on an initial set of 15 independent cases. All images were evaluated on a DICOM viewer workstation with OsiriX 64-bit, software *(www.osirix-viewer.com)* across the features in the image feature library in the equilibrium (70-second acquisition) and precontrast phases where available and necessary. Both the training (L.A. and M.D.K., with 4 and 6 years of experience, respectively) and validation (L.A. and R.L.K., each with 12 years of experience) sets were independently reviewed by two board-certified radiologists, and Cohen kappa statistics were calculated. Imaging features were assessed in three consecutive sections that spanned the largest axial diameter of the tumors. Discrepant interpretations were subsequently resolved in consensus (Table E2 [online]).

RSS Construction

As was previously described, a global map that linked image features to transcript expression levels was created (5). Briefly, we identified sets of transcripts that significantly correlated with each imaging trait (hereafter referred to as trait-associated genes). Thus, we evaluated the correlation of the $\log_2$ (Cy5/Cy3) expression ratio for every cDNA clone with each imaging trait by using a Spearman rank correlation coefficient. To assess significance and control for multiple hypothesis testing, we generated 3000 random permutations of the imaging trait values and recalculated the correlation coefficient to each cDNA element. The distributions generated from these calculations were used to determine correlation coefficients corresponding to $P < .05$. All cDNA elements with absolute correlation coefficients greater than this cut-off were included in the trait-associated gene sets.

Next, for consistency with the study by Zhao et al (10), the RRS, a semiquantitative radiogenomic surrogate for the SPC gene signature, was constructed from the 70 CCRCCs in the training set by using the 28 stage-independent image features after seven stage-dependent traits were removed from the original 35 image feature library (Table E1 [online]). Similar to Zhao et al, the gene expression matrix was populated with the genes whose absolute Cox score exceeded the threshold as previously established. Survival analysis was performed on the first principal component to confirm the prognostic value of the SPC gene signature as previously described by Zhao et al (10). Multivariate regression analysis of gene expression data was used to select the top imaging traits (11). As was previously described, the patient-wise gene expression distance matrix was calculated by using the Pearson correlation coefficient and the equation $d_{ij} = [2*(1-r_{ij})]^{1/2}$ for each r_{ij} entry in the $n \times n$ correlation matrix (for n patients) (11). The RRS was then calculated by performing multivariate linear regression between the top eigenvector of the patient-wise gene expression distance matrix and by using the four top imaging traits that accounted for the greatest variance (11). To determine that this model was not randomly identified as the best model, bootstrap analysis was performed with 100 000 resamples ($P < .001$).

Receiver Operator Characteristic Analysis

To evaluate the ability of the RRS to predict the SPC risk score, receiver operating characteristic (ROC) curve analysis was performed to identify the optimal threshold for maximizing sensitivity and specificity. The training set was divided into two groups on the basis of the cutoff from ROC curve analysis: low and high risk score groups. The patients in the validation set were similarly classified into low and high risk score groups on the basis of their risk scores by using the cutoff established in the training set. Survival times of the subgroups in the training and independent validation sets were compared by using Kaplan-Meier survival analysis.

Statistical Analysis

Principal component and Pearson correlation analysis were performed with Matlab (MathWorks, Natick, Mass) and R *(http://www.r-project.org/)* software. Multivariate linear regression, Cox regression modeling, diagnostic accuracy, Cohen kappa, Kaplan-Meier survival analysis with log rank tests, and ROC curve analysis were performed with R, Matlab, Statistica (StatSoft, Tulsa, Okla), and Python *(www.python.org)* software. Two-way average-linkage hierarchical clustering of expression profile data was applied and visualized with Cluster 3.0 *(http://bonsai.hgc.jp/~mdehoon/software/cluster/)* and TreeView *(http://jtreeview.sourceforge.net/)*.

Results

Patient Characteristics

No significant differences were found between the training and validation sets with respect to patient sex, patient age, disease stage, disease grade, WHO performance status, follow-up time, and disease-specific death. At the time of analysis, the number of disease-specific deaths for the training and validation sets was 32 and 29, respectively. Detailed patient characteristics are summarized in Table 1.

Gene Expression Profiling

Applying the filtering criteria to the training set resulted in a total of 5332 cDNA elements. From this, 217 transcripts representing 139 genes from the SPC signature were identified and extracted. A complete list of these transcripts, with Unigene cluster ID, gene description, and gene symbol, is shown in Table E1 (online).

Development of the RSS

A radiogenomic association map between 28 well-measured and variably expressed features on contrast-enhanced CT images and the gene expression patterns of 5332 well-measured and variably expressed transcripts that represented 4825 unique genes from the 70 CCRCCs in the training set was constructed and revealed that a large percentage (79.0%) of the global gene expression program in CCRCC could be reconstructed from this discrete population of image features (Table E2 [online]). Next, to define the image analog of the SPC gene signature, multivariate regression analysis of gene expression analysis identified a relationship between the SPC score and the expression of four CT features, which we termed the RRS. The RRS is a linear combination of the following four stage- and grade-independent imaging traits: pattern of tumor necrosis (trait 17), tumor transition zone (trait 26), tumor-parenchyma interaction (trait 30), and tumor-parenchyma interface (trait 31) (Table E2 [online]). The multivariate regression equation resulting from multivariate regression analysis of gene expression selection of the top four traits is given with the equation $Y = \beta_1 X_{17} + \beta_2 X_{26} + \beta_3 X_{30} + \beta_4 X_{31} + b$, where $b = -0.187$, $\beta_1 = 0.03591$, X_{17} = trait 17, $\beta_2 = 0.113$, X_{26} = trait 26, $\beta_3 = -0.124$, X_{30} = trait 30, $\beta_4 = -0.08016$, and X_{31} = trait 31 (corrected analysis of variance P value $< .001$) (Fig 3).

Figure 3

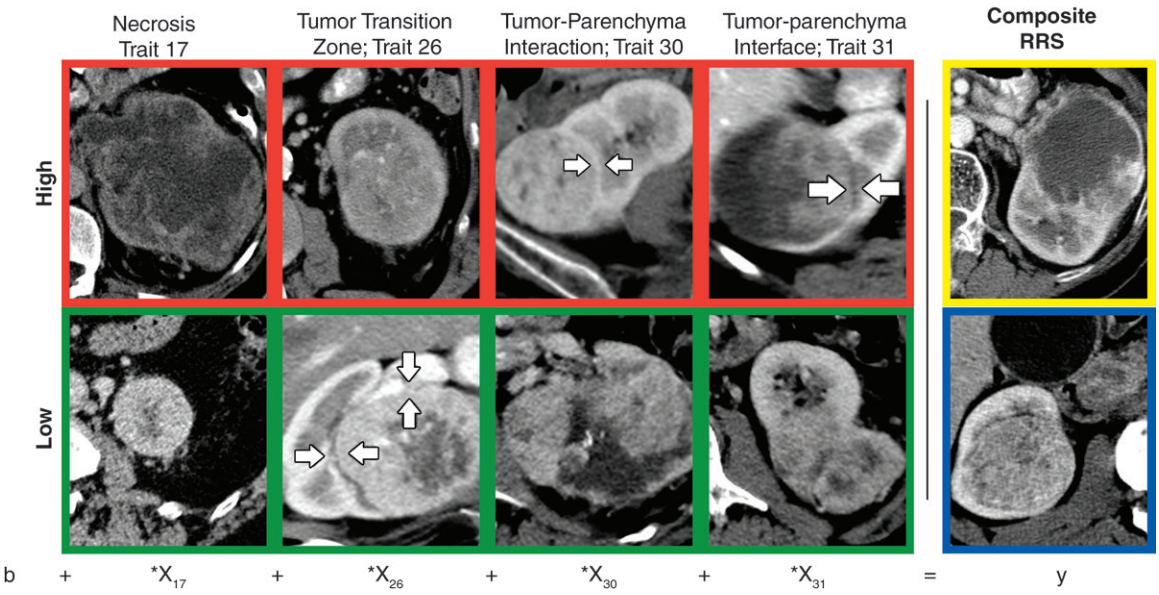

Figure 3: Definition of the RRS phenotype. CT images show the four imaging traits that constitute the RRS, with examples of high (red) and low (green) scores for each imaging feature, and the composite high- (yellow) and low- (blue) risk score phenotype. From the left, trait 17 (first column) assesses the quartile percentage of tumor necrosis (the low RRS example image shows a 3.2-cm exophytic mass with a minimal amount of central necrosis); trait 26 (second column) assesses a sharp (arrows) versus infiltrating transition zone between tumor and renal parenchymal tissue; trait 30 (third column) assesses the presence or absence of a discrete rim of enhancement circumscribing the tumor (arrows); and trait 31 (fourth column) assesses the presence or absence of a hypoattenuating rim circumscribing the tumor (arrows). For each trait, the linear equation and coefficients that define the RRS are listed, where b = −0.187, β_1 = 0.03591, X_{17} = trait 17, β_2 = 0.113, X_{26} = trait 26, β_3 = −0.124, X_{30} = trait 30, β_4 = −0.08016, X_{31} = trait 31, and y = RRS.

RRS Tracks SPC Gene Signature and Predicts Outcome in Patients with CCRCC

The RRS significantly correlated with expression of the SPC risk score gene signature (R = 0.57, $P < .001$), confirming its relationship to this quantitative multigene assay (Fig E1 [online]). ROC analysis identified the optimal classification of patients into risk groups (high vs low) at a RRS cut-off value of −0.01318 (Fig E2 [online]). In addition, although the RRS was derived from 139 of 259 of the most variably expressed SPC risk score genes and, thus, was not devised to explicitly track the full 259 genes of the nominal SPC risk score (a weighted composite of the expression levels of all 340 component transcripts), we found that the RRS significantly correlated with the nominal SPC risk score, as well (R = 0.48, $P < .001$), confirming that our assay tracks the core SPC risk score (10). The high RRS group had significantly worse survival than the low RRS group on the basis of Kaplan-Meier estimates ($P < .001$), with a median survival of 32 months in the high RRS group versus 150 months in the low RRS group (Fig 4, *A*). Further, classification of patients into "good" and "poor" SPC risk score prognosis groups revealed a comparable outcome profile (P = .0263) (Fig 4, *B*). Comparison of the observed risk score predictor against permuted samples (10^5 permutations) confirmed that the strong relationship between risk score and both the SPC gene signature ($P < .001$) and overall survival ($P < .01$) was unlikely due to chance. Finally, the RRS classification also strongly mirrored the classification of SPC risk score patients (accuracy, 70.1%; $P < .001$). In total, these findings confirmed that our image-based assay was reflective of the tissue-based assay it targeted, tracking both the expression of the SPC risk score genes and the SPC risk score and its classification of samples (2).

To further validate our image-based assay, we predicted the relationship between the radiogenomic risk score and the SPC risk score classification in an independent set of 70 prospectively collected patients with CCRCC. The correlation between the SPC risk score genes and the RRS persisted in the validation set (R = 0.45, $P < .001$) despite the fact that the SPC risk score used in the training set was derived from a custom microarray that contained probe sets that were not present in the newer generation microarray platform used in the validation set. These patients were also evaluated against clinical outcome and placed into either a high or low RRS group by using the threshold established in the training data (n = 77). Survival analysis confirmed that the high RRS group had significantly lower disease-specific survival rates than did the low RRS group ($P < .001$), with a median survival time of 40 months for the low RRS group and more than 120 months for the high low

Figure 4

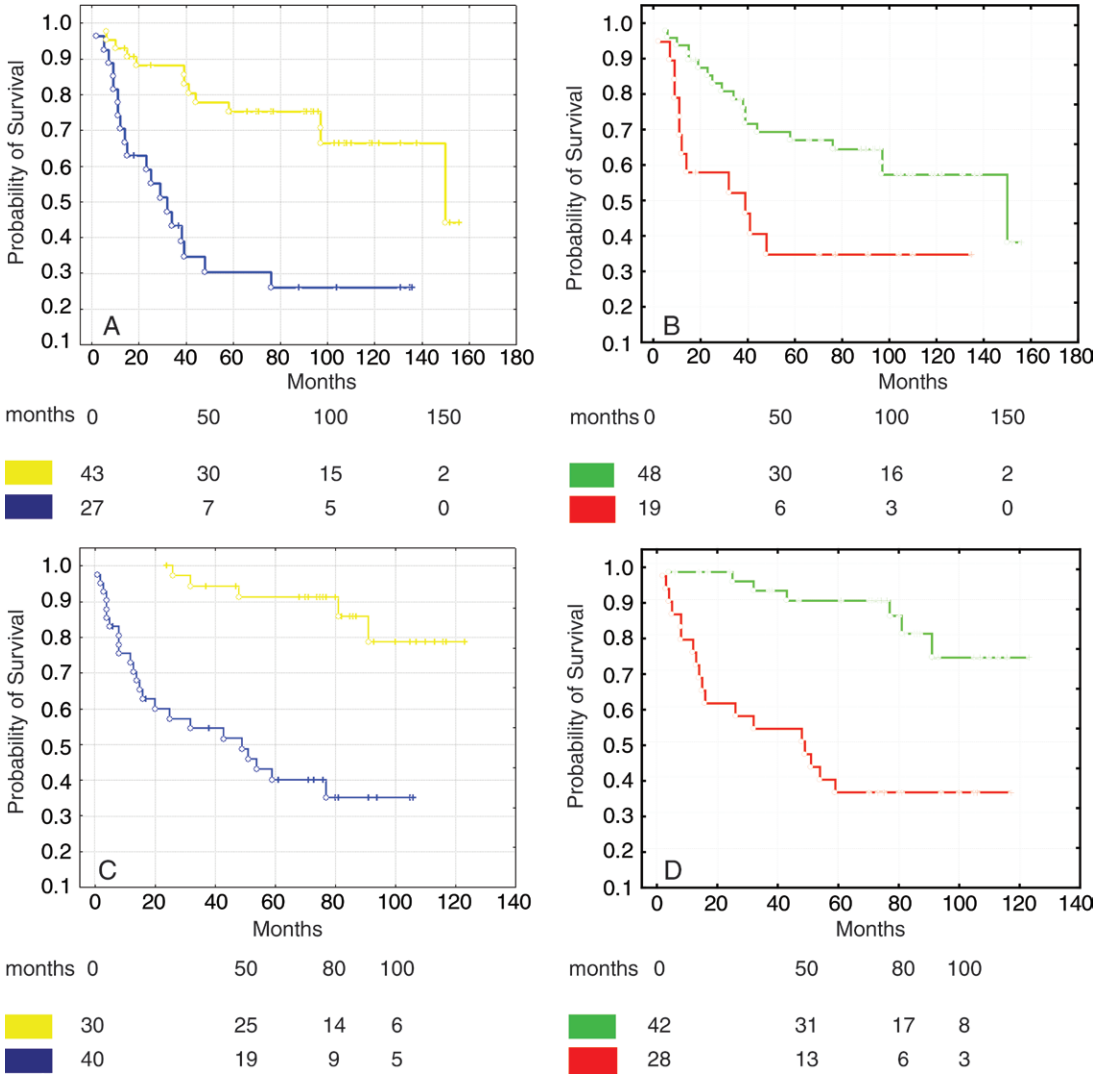

Figure 4: Characteristics of the RRS. *A,* Kaplan-Meier curves for disease-specific survival in the training set show the high (blue line) and low (yellow line) RRS groups ($P = .00147$). *B,* Kaplan-Meier curves for disease-specific survival in the training set show the good (green line) and poor (red line) prognosis SPC risk score ($P = .0263$). *C,* Kaplan-Meier curves for disease-specific survival in the validation set show the probability of disease-specific survival for the high (blue line) and low (yellow line) RRS groups ($P = .00024$). *D,* Kaplan-Meier curves for disease-specific survival in the validation set show the probability of disease-specific survival for the good (green line) and poor (red line) SPC groups ($P = .00006$).

RRS group (Fig 4, *C*). Survival analysis performed on the basis of SPC risk score in the validation set also revealed a similar outcome profile (Fig 4, *D*). Again, RRS classification strongly mirrored that of SPC risk score (accuracy, 68.6%; $P < .001$). Finally, a multivariate Cox proportional hazards model demonstrated that the risk score, similar to the SPC risk score, was independent of tumor stage, tumor grade, and performance status (Cox model likelihood ratio test, $P < .03$, hazard ratio, 1.57) (Table 2). There was substantial interobserver agreement of the RRS as measured by Cohen kappa statistic, with 0.7645 ± 0.0784 for the training set (lower limit, 0.6109; upper limit, 0.9181; and eight discrepant cases that were resolved in consensus) and 0.8192 ± 0.0652 for the validation set (lower limit, 0.6915; upper limit, 0.9469; and seven discrepant cases that were resolved in consensus) (14).

Discussion

In summary, we demonstrate that targeted noninvasive image-based molecular assays (SOMA) that track targeted quantitative molecular phenotypes

Table 2

Multivariate Cox Survival Regression (Validation Cohort)

Predictor Variable	Univariate *P* Value	Multivariate *P* Value	Multivariate HR
RRS	.0001	.04	3.32
Disease stage	<.001	.01	1.87
WHO performance	.001	.02	1.78
Disease grade	.0004	.01	1.77

Note.—HR = hazard ratio.

and assays can be designed in patients with CCRCC. Recently, Karlo et al (15) explored associations between nucleotide variations in five genes and eight CT features in patients with renal cell carcinoma. In our study, we sought to construct a complex, multifeature imaging predictor by using a multigene predictive gene expression signature (SPC risk score). We prospectively designed a semiquantitative noninvasive image assay constructed from an initial screen of a library of CT features against a previously established prognostic quantitative multigene assay in patients with CCRCC. Similar to the SPC risk score molecular phenotype it targets, the RRS SOMA expresses prognostic power and is independent of disease stage, WHO classification, and disease grade, and it maintains high sample classification accuracy. Importantly, the RRS was validated in an independent cohort of patients who we prospectively collected and molecularly profiled, where it continued to demonstrate significant association with the SPC risk score, strong classification accuracy, and an ability to stratify patients on the basis of disease-specific death independent of stage, WHO classification, and disease grade (16).

The SOMA concept is generalizable and, in principle, agnostic of disease type and imaging modality (eg, positron emission tomography, magnetic resonance imaging, CT, and optical imaging) and applicable to different molecular phenotype classes (eg, copy number variations, gene expression signatures, and metabolic phenotypes). Although we focus on renal cell carcinoma, the strength and breadth of our results are encouraging and speak to the robustness of both the RRS and the approach in general. A number of prognostic gene signatures have been identified in renal cell cancer; however, we focused on the SPC risk score for proof of concept because of its strong similarity to prognostic quantitative multigene assays that were recently developed for clinical use, thus approximating a potential real-world application (1,17,18). For example, a number of quantitative multigene assays with prognostic and predictive components are in clinical use in patients with other tumor types, such as breast and prostate cancer, for whom images are routinely obtained for pretreatment evaluation (18–20). These and other similar tests suffer from some of the limitations associated with many tissue-based genomic tests in general, such as cost and morbidity associated with invasive procedures for tissue acquisition and are ideal for translation into SOMAs.

While recent work highlights the potential importance of intra- and intertumoral genomic heterogeneity in tissue samples, its overall impact on clinical practice remains to be determined because the current standard clinical practices and Clinical Laboratory Improvement Amendments–certified genomic tests are based on total tissue samples from a single lesion, similar to the radiogenomic risk score (3,20–22). Further, studies have shown that aggregate expression levels of RNA from a single site in the primary tumor alone are powerful predictors of eventual metastasis and death (23). Although there is evidence that radiogenomic approaches can provide sufficient sensitivity to detect differences in molecular profiles at an intratumoral level, further studies are needed to evaluate the sensitivity and capabilities of imaging technologies to detect any causal links between intratumoral heterogeneity and tumor phenotype (5,24). In the future, when single cell isolation studies become technically feasible and cost effective, we expect that there will be increased sensitivity and specificity of genomic biomarkers and a potential transition from inter- to intratumoral-based genomic tests; in which case, the approach proposed herein should still be applicable with the parallel progression from intertumoral-based SOMAs to more spatially resolved intratumoral-based SOMAs. Additionally, although "expert level" qualitative or semiquantitative imaging traits remain the reference standard for identifying complex features and subtyping different tumors in the clinic, as computer vision and quantitative feature extraction methodologies improve and become validated and standardized, we expect automated feature extraction will further improve the efficiency of the radiogenomic assay workflow.

Although the physiologic and biologic interpretability of the RRS is a favorable strength of this radiogenomic biomarker, a potential limitation of this study is that the current implementation of image feature detection is not automated. While it would be ideal to capture all features with automated processes and almost completely remove human interaction, it is important to remember that, first, the vast majority of clinical radiologic interpretation is still held to the standard of the human eye, and, second, current automated image analysis procedures are still relatively limited in their ability to capture complex patterns beyond standard physiologic or textural features and clearly lag human pattern recognition capabilities. Additionally, the majority of published radiogenomic studies to date have relied on human experts for feature scoring, having demonstrated strong correlation with underlying genetic signatures, strong

reproducibility, and an ability to capture complex features (5,7–9,25–28). Similarly, we are encouraged that interpretation of the RRS was robust as assessed by interobserver agreement and, further, was consistent with our previous reports, supporting the robustness of its evaluation in clinical practice. Nonetheless, we are optimistic that with continued developments in segmentation and automated feature analysis, it will become increasingly possible to automate parts, or all, of this framework (29). Anticipated future advancements in the state-of-the-art automated feature extraction of renal masses will likely contribute to improved consistency, reproducibility, and throughput in the development and implementation of SOMAs.

The stepwise process for constructing SOMAs served to bridge multiple biologic spatial scales from subcellular transcriptional signatures to cellular and tissue histopathologic characteristics and tissue- and organ-level characteristics by CT, findings that were then linked to clinical outcomes and treatment response. Part of the success of our approach may be attributable to the fact that the RRS predictor consists of a unique combination of physiologic and tumor-parenchyma interaction-based imaging features that are biologically and oncologically relevant. Such insight serves to highlight the importance of these previously unheralded image phenotypes that can be immediately implemented in the daily clinical evaluation of these tumors by revealing the critical relationships between tissue physiologic and morphologic characteristics, transcriptional patterns, and prognosis.

While the gross majority of biomarker identification studies focus on single measurements or features, our results suggest that, to capture complexities of biologic processes, it is likely necessary to obtain and integrate multidimensional measures. The introduction of the RRS for CCRCC and the concept of a noninvasive imaging assay as an application of radiogenomic approaches for biomarkers may have useful future applications for detecting and tracking diseases, with exciting future applications for renal cell carcinoma, as well as potential applications to other diseases. This approach for radiogenomic biomarker identification further ameliorates the tissue burden of strictly tissue-based biomarkers and may help defray the cost and time associated with repeated tissue acquisition. In the future, such limitations could potentially be ameliorated with a SOMA-based approach, in which target molecular or clinical phenotypes can be rapidly designed and screened in silico in actual human data sets.

Acknowledgment: The authors gratefully acknowledge funding from the Society of Interventional Radiology Foundation Student Research Grant.

Disclosures of Conflicts of Interest: N.J. disclosed no relevant relationships. **E.J.** disclosed no relevant relationships. **M.Z.** disclosed no relevant relationships. **R.K.** Activities related to the present article: disclosed no relevant relationships. Activities not related to the present article: founder and shareholder of Imaging Endpoints Research and Core Lab. Other activities: disclosed no relevant relationships. **L.A.** disclosed no relevant relationships. **H.Z.** disclosed no relevant relationships. **R.T.S.** disclosed no relevant relationships. **R.J.T.** disclosed no relevant relationships. **S.B.** disclosed no relevant relationships. **J.D.B.** disclosed no relevant relationships. **B.I.** disclosed no relevant relationships. **M.D.K.** disclosed no relevant relationships.

References

1. Brannon AR, Reddy A, Seiler M, et al. Molecular stratification of clear cell renal cell carcinoma by consensus clustering reveals distinct subtypes and survival patterns. Genes Cancer 2010;1(2):152–163.
2. Fan C, Oh DS, Wessels L, et al. Concordance among gene-expression-based predictors for breast cancer. N Engl J Med 2006;355(6):560–569.
3. Gerlinger M, Rowan AJ, Horswell S, et al. Intratumor heterogeneity and branched evolution revealed by multiregion sequencing. N Engl J Med 2012;366(10):883–892.
4. Kreso A, O'Brien CA, van Galen P, et al. Variable clonal repopulation dynamics influence chemotherapy response in colorectal cancer. Science 2013;339(6119):543–548.
5. Diehn M, Nardini C, Wang DS, et al. Identification of noninvasive imaging surrogates for brain tumor gene-expression modules. Proc Natl Acad Sci U S A 2008;105(13):5213–5218.
6. Gevaert O, Xu J, Hoang CD, et al. Non-small cell lung cancer: identifying prognostic imaging biomarkers by leveraging public gene expression microarray data--methods and preliminary results. Radiology 2012;264(2):387–396.
7. Jamshidi N, Diehn M, Bredel M, Kuo MD. Illuminating radiogenomic characteristics of glioblastoma multiforme through integration of MR imaging, messenger RNA expression, and DNA copy number variation. Radiology 2014;270(1):1–2.
8. Segal E, Sirlin CB, Ooi C, et al. Decoding global gene expression programs in liver cancer by noninvasive imaging. Nat Biotechnol 2007;25(6):675–680.
9. Yamamoto S, Korn RL, Oklu R, et al. ALK molecular phenotype in non-small cell lung cancer: CT radiogenomic characterization. Radiology 2014;272(2):568–576.
10. Zhao H, Ljungberg B, Grankvist K, Rasmuson T, Tibshirani R, Brooks JD. Gene expression profiling predicts survival in conventional renal cell carcinoma. PLoS Med 2006;3(1):e13.
11. Zapala MA, Schork NJ. Multivariate regression analysis of distance matrices for testing associations between gene expression patterns and related variables. Proc Natl Acad Sci U S A 2006;103(51):19430–19435.
12. Du P, Kibbe WA, Lin SM. lumi: a pipeline for processing Illumina microarray. Bioinformatics 2008;24(13):1547–1548.
13. Kuo MD, Gollub J, Sirlin CB, Ooi C, Chen X. Radiogenomic analysis to identify imaging phenotypes associated with drug response gene expression programs in hepatocellular carcinoma. J Vasc Interv Radiol 2007;18(7):821–831.
14. Viera AJ, Garrett JM. Understanding interobserver agreement: the kappa statistic. Fam Med 2005;37(5):360–363.
15. Karlo CA, Di Paolo PL, Chaim J, et al. Radiogenomics of clear cell renal cell carcinoma: associations between CT imaging features and mutations. Radiology 2014;270(2):464–471.
16. Kuo MD, Jamshidi N. Behind the numbers: Decoding molecular phenotypes with radiogenomics--guiding principles and technical considerations. Radiology 2014;270(2):320–325.
17. Zhao H, Zongming Ma, Tibshirani R, Higgins JP, Ljungberg B, Brooks JD. Alteration of gene expression signatures of cortical differentiation and wound response in lethal clear cell renal cell carcinomas. PLoS One 2009;4(6):e6039.
18. Kittaneh M, Montero AJ, Glück S. Molecular profiling for breast cancer: a comprehensive review. Biomark Cancer 2013;5:61–70.

19. Clark-Langone KM, Sangli C, Krishnakumar J, Watson D. Translating tumor biology into personalized treatment planning: analytical performance characteristics of the Oncotype DX Colon Cancer Assay. BMC Cancer 2010;10:691.
20. Knezevic D, Goddard AD, Natraj N, et al. Analytical validation of the Oncotype DX prostate cancer assay - a clinical RT-PCR assay optimized for prostate needle biopsies. BMC Genomics 2013;14:690.
21. Cardoso F, Van't Veer L, Rutgers E, Loi S, Mook S, Piccart-Gebhart MJ. Clinical application of the 70-gene profile: the MINDACT trial. J Clin Oncol 2008;26(5):729–735.
22. Cronin M, Sangli C, Liu ML, et al. Analytical validation of the Oncotype DX genomic diagnostic test for recurrence prognosis and therapeutic response prediction in node-negative, estrogen receptor-positive breast cancer. Clin Chem 2007;53(6):1084–1091.
23. Gupta RA, Shah N, Wang KC, et al. Long non-coding RNA HOTAIR reprograms chromatin state to promote cancer metastasis. Nature 2010;464(7291):1071–1076.
24. Barajas RF Jr, Hodgson JG, Chang JS, et al. Glioblastoma multiforme regional genetic and cellular expression patterns: influence on anatomic and physiologic MR imaging. Radiology 2010;254(2):564–576.
25. Gutman DA, Cooper LA, Hwang SN, et al. MR imaging predictors of molecular profile and survival: multi-institutional study of the TCGA glioblastoma data set. Radiology 2013;267(2):560–569.
26. Nicolasjilwan M, Hu Y, Yan C, et al. Addition of MR imaging features and genetic biomarkers strengthens glioblastoma survival prediction in TCGA patients. J Neuroradiol 2014;42(4):212–221.
27. Yamamoto S, Maki DD, Korn RL, Kuo MD. Radiogenomic analysis of breast cancer using MRI: a preliminary study to define the landscape. AJR Am J Roentgenol 2012;199(3):654–663.
28. Zinn PO, Mahajan B, Sathyan P, et al. Radiogenomic mapping of edema/cellular invasion MRI-phenotypes in glioblastoma multiforme. PLoS One 2011;6(10):e25451.
29. Yamamoto S, Han W, Kim Y, et al. Breast cancer: radiogenomic biomarker reveals associations among dynamic contrast-enhanced MR imaging, long noncoding RNA, and metastasis. Radiology 2015;275(2):384–392.